PROCEEDINGS OF SPIE

SPIEDigitalLibrary.org/conference-proceedings-of-spie

The TolTEC camera: an overview of the instrument and in-lab testing results

Wilson, Grant, Abi-Saad, Sophia, Ade, Peter, Aretxaga, Itziar, Austermann, Jason, et al.

Grant W. Wilson, Sophia Abi-Saad, Peter Ade, Itziar Aretxaga, Jason Austermann, Yvonne Ban, Joseph Bardin, James Beall, Marc Berthoud, Sean Bryan, John Bussan, Edgar Castillo, Miguel Chavez, Reid Contente, N. S. DeNigris, Bradley Dober, Miranda Eiben, Daniel Ferrusca, Laura Fissel, Jiansong Gao, Joseph E. Golec, Robert Golina, Arturo Gomez, Sam Gordon, Robert Gutermuth, Gene Hilton, Mohsen Hosseini, Johannes Hubmayr, David Hughes, Stephen Kuczarski, Dennis Lee, Emily Lunde, Zhiyuan Ma, Hamdi Mani, Philip Mauskopf, Michael McCrackan, Christopher McKenney, Jeffrey McMahon, Giles Novak, Giampaolo Pisano, Alexandra Pope, Amy Ralston, Ivan Rodriguez, David Sánchez-Argüelles, F. Peter Schloerb, Sara Simon, Adrian Sinclair, Kamal Souccar, Ana Torres Campos, Carole Tucker, Joel Ullom, Eric Van Camp, Jeff Van Lanen, Miguel Velazquez, Michael Vissers, Eric Weeks, Min S. Yun, "The TolTEC camera: an overview of the instrument and in-lab testing results," Proc. SPIE 11453, Millimeter, Submillimeter, and Far-Infrared Detectors and Instrumentation for Astronomy X, 1145302 (13 December 2020); doi: 10.1117/12.2562331

SPIE.

Event: SPIE Astronomical Telescopes + Instrumentation, 2020, Online Only

The TolTEC camera: An overview of the instrument and in-lab testing results

Grant W. Wilson[a], Sophia Abi-Saad[a], Peter Ade[b], Itziar Aretxaga[c], Jason Austermann[d], Yvonne Ban[a], Joseph Bardin[e], James Beall[d], Marc Berthoud[f], Sean Bryan[k], John Bussan[m], Edgar Castillo-Domínguez[c], Miguel Chavez[c], Reid Contente[a], N. S. DeNigris[a], Bradley Dober[d], Miranda Eiben[a], Daniel Ferrusca[c], Laura Fissel[h], Jiansong Gao[d], Joseph E. Golec[j], Robert Golina[f], Arturo Gomez[c], Sam Gordon[l], Robert Gutermuth[a], Gene Hilton[d], Mohsen Hosseini[e], Johannes Hubmayr[d], David H. Hughes[c], Stephen Kuczarski[a], Dennis Lee [f], Emily Lunde[g], Zhiyuan Ma[a], Hamdi Mani[g], Philip Mauskopf[g], Michael McCrackan[a], Christopher McKenney[d], Jeffrey McMahon[j], Giles Novak[f], Giampaolo Pisano[b], Alexandra Pope[a], Amy Ralston[a], Ivan Rodriguez[c], David Sánchez-Argüelles[c], F. Peter Schloerb[a], Sara Simon[i], Adrian Sinclair[g], Kamal Souccar[a], Ana Torres Camposana[c], Carole Tucker[b], Joel Ullom[d], Eric Van Camp[f], Jeff Van Lanen[d], Miguel Velazquez[c], Michael Vissers[d], Eric Weeks[g], and Min S. Yun[a]

[a]Dept. of Astronomy, University of Massachusetts, Amherst, MA, USA;
[b]Cardiff University, Cardiff, Wales;
[c]Instituto Nacional de Astrofísica, Óptica y Electrónica (INAOE), Luis Enrique Erro 1, Sta. Ma. Tonantzintla, 72840, Puebla, Mexico;
[d]National Institute of Standards and Technology, Boulder, CO, USA;
[e]Dept. of Electrical Engineering, University of Massachusetts, Amherst, MA, USA;
[f]Center for Interdisciplinary Exploration and Research in Astrophysics (CIERA) and Department of Physics and Astronomy, Northwestern University, Evanston, IL, USA;
[g]Dept. of Physics, Arizona State University, Tempe, AZ, USA;
[h]Dept. of Physics, Engineering Physics & Astronomy, Queen's University, Kingston, ON, Canada;
[i]Department of Physics, University of Michigan, Ann Arbor, MI, USA;
[j]Dept. of Physics, University of Chicago, Chicago, IL, USA;
[k]School of Electrical, Computer, and Energy Engineering, Arizona State University, Tempe, AZ USA;
[l]School of Earth and Space Exploration, Arizona State University, Tempe, AZ USA;
[m]Northwestern University Research Shop, Northwestern University, Evanston, IL, USA;
[n]Department of Physics, La Sapienza University of Rome, Italy;

ABSTRACT

TolTEC is a three-band imaging polarimeter for the Large Millimeter Telescope. Simultaneously observing with passbands at 1.1mm, 1.4mm and 2.0mm, TolTEC has diffraction-limited beams with FWHM of 5, 7, and 11 arcsec, respectively. Over the coming decade, TolTEC will perform a combination of PI-led and Open-access Legacy Survey projects. Herein we provide an overview of the instrument and give the first quantitative measures of its performance in the lab prior to shipping to the telescope in 2021.

Keywords: mm-wavelength, camera, kinetic inductance detector, Large Millimeter Telescope

Send correspondence to G. Wilson:
Email: wilson@astro.umass.edu, Telephone: 1 413 545 0460

Millimeter, Submillimeter, and Far-Infrared Detectors and Instrumentation for Astronomy X,
edited by Jonas Zmuidzinas, Jian-Rong Gao, Proc. of SPIE Vol. 11453, 1145302
 · doi: 10.1117/12.2562331

1. INTRODUCTION

The TolTEC camera is a 3-band imaging polarimeter being built as a facility instrument for the Large Millimeter Telescope (LMT).[1] The camera utilizes 7718 kinetic inductance detectors (KIDs) in three arrays to provide simultaneous imaging in bands centered at 1.1 mm, 1.4 mm, and 2.0 mm wavelength. The active pixel count of the camera, when combined with the 50 m diameter LMT, will result in a combination of mapping speed and resolution that is unmatched by any other millimeter-wavelength facility.

Once installed on the LMT, the TolTEC Project will undertake a series of ten Legacy Surveys, each using 100 hours of telescope time, whose data will be made publicly available. The first four of these surveys were designed through a series of public webinars and meetings in 2018.[2] They are: the Fields in Filament Survey - a survey of the magnetic fields via polarized dust emission in star-forming regions; the Clouds to Cores Survey - a survey of the core mass function in several molecular clouds; the Ultra-Deep Survey - a survey of metal production and star formation in galaxies at the 1.1mm confusion limit; and the Large Scale Structure Survey - a survey of the distribution and prevalence of ULIRGs and SMGs over 50 deg^2.

The full TolTEC instrument was integrated and has been undergoing testing at UMass since late 2019. As described in Section 2.3, a subtle but vexing problem with the dichroic beam splitters, which we ultimately traced to a fabrication issue, required a series of cooldowns and optical tests of the instrument during much of 2020. In addition, the Covid-19 pandemic led to a shutdown of instrument hardware activities for 3 months of 2020 followed by a reduced level of person-power in the lab for testing. Consequently, we now expect to ship TolTEC to the LMT in 2021, once the Covid-19 pandemic allows, for commissioning and first science.

The optical design and sensitivity estimates for TolTEC were originally described in Bryan *et al.* 2018.[3] In this paper we report on the status of the instrument, provide an overview of its major subsystems, and provide lab-testing results that demonstrate the overall soundness of the system design and performance.

2. INSTRUMENT OVERVIEW

2.1 Cryogenics Design

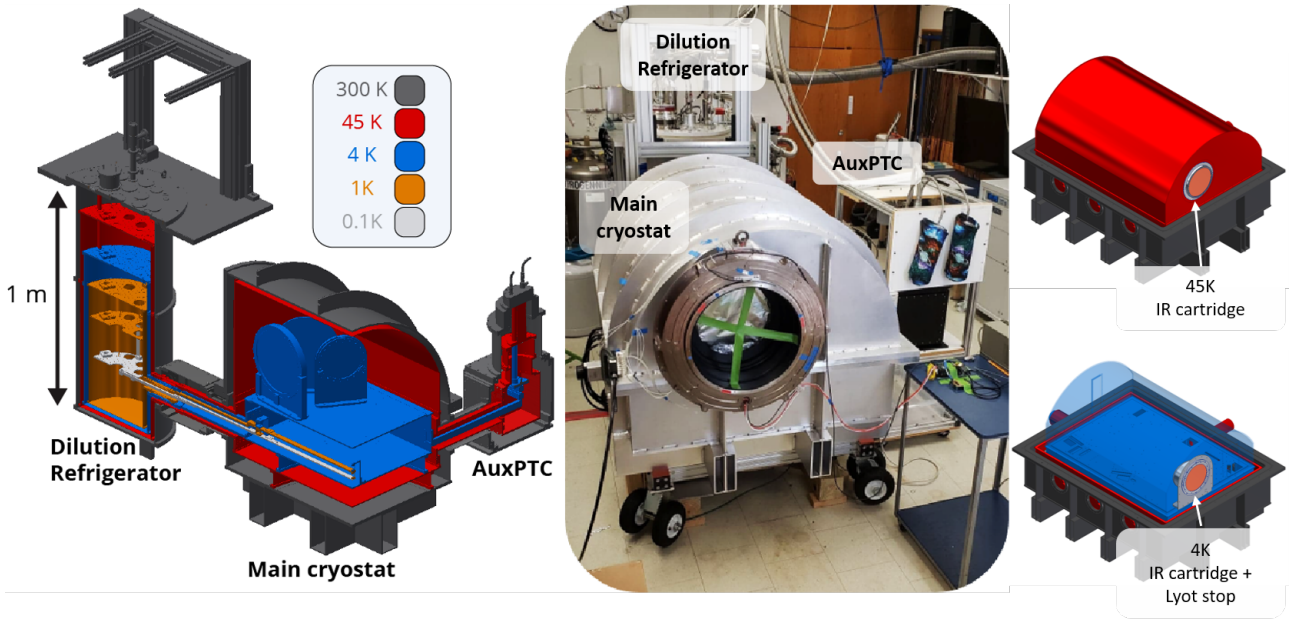

Figure 1. (Left:) Cutaway of TolTEC's cryostat and two cooling systems to show the four thermal stages interior to the outer vacuum shell. (Middle:) A photo of the instrument in the lab at UMass with the Half-wave plate rotator mounted at the window of hte cryostat. (Right): CAD views of the 45K (top) and 4K (bottom) stages with their IR blocking filter cartridges.[4]

TolTEC features four thermal stages cooled by two cryocoolers operating in tandem. For simplicity, we refer to the four stages as the 45 K, 4 K, 1 K and 100 mK stages, though the actual stage temperatures vary due to thermal gradients in the system. The bulk of the 45 K and 4 K stages are cooled by a Cryomech 415 Pulse Tube Cooler, henceforth referred to as the Auxiliary Pulse Tube Cooler (AuxPTC). For the detector arrays (100 mK) and their supports (1 K), we use an Oxford Instruments Triton 2016 dilution refrigerator (DR). The DR also offers additional cooling power for the two warmer stages (45 K, 4 K). The cryostat's design, and large size, was driven by the 300 mm diameter window and the area of the 4 K optics bench (1.3 m by 1.0 m) required to fit three detector arrays and their optics. We settled on a nested shell design (see Figure 1) to facilitate modifications and repairs to the system by separating the cryogenic, electronic and optical subsystems as much as possible. Each subsystem resides in relative isolation for debugging while leaving flexibility for future modifications. For a more detailed discussion of the cryogenic system design and operation, please refer to DeNigris *et al.* 2020.[4]

The full system takes approximately one week to reach a stable base temperature as well as one week to reach room temperature after ending the cooling cycle. Once cold, the three focal planes have operating temperatures of 145, 150, and 155 mK, with the coolest of the three being physically closest to the dilution refrigerator. The dilution refrigerator's mixing chamber typically runs at 55 mK and the still at 0.8 K, which implies that we are not using the full cooling capacity of the dilution refrigerator. Instead, we find that our achievable array temperatures are limited by the thermal gradients in the copper bus bars between the arrays and the mixing chamber, which is consistent with our cryostat thermal model. These array temperatures meet our goal of $T < 200$ mK to avoid excess thermal quasiparticles and $T > 100$ mK to avoid excess two-level system (TLS) noise in the detectors. As of October 2020, our longest continuous operation of the system was one month wherein we were able to observe the long-term stability of the 100 mK stage. We measure variations in the array temperatures of $\lesssim 1$ mK over the course of 20 days during this cooldown.

The excess cooling capacity in our 1 K cryogenic stage gives us the option to add cold (1.2 K) baffling at strategic points in the cryostat. We have done this in two places to reduce the background radiative loading on the detector arrays. Early in our in lab testing phase we found that the detector resonances were not achieving the desired quality factors due to light leaks from scattering in the 1 K detector assembly. To solve this, we closed the front of the 1 K copper supports and added a blackened, aluminum baffle that attaches to the back of the 1 K filter holder and surrounds the detector feedhorns on the sides. We also added a 1 K blackened baffle at the Lyot stop through which light enters the 4 K optical volume (see Figure 3). This baffle was constructed from a rolled sheet of oxygen-free high-conductivity copper that was then blackened using Stycast and carbon-infused cloth. We used carbon fiber standoffs to mechanically mount the baffle to the 4 K optics bench while attaching the rolled copper sheet to a 1 K thermal link to the dilution refrigerator.

2.2 Detectors and Array Assemblies

TolTEC uses arrays of microwave-multiplexed Kinetic Inductance Detectors (KIDs)[5] developed at NIST. The detector and feedhorn design are described in Austermann *et al.* 2018[6] and will be further described in paper **#11453-10** in these proceedings. Here we focus on the array assemblies and their mounting. TolTEC has three independent detector array assemblies, each with their own mechanical mounts, thermal straps, low noise amplifier assemblies, and readout electronics. We refer to the assemblies as the 1.1mm array, the 1.4mm array, and the 2.0mm array. A schematic exploded view of the 1.1mm array's assembly is shown in Figure 2.

The detector assemblies are made up of three nested assemblies at 150 mK, 1.2 mK, and 5 K, with the array of detectors mounted at the innermost stage. Each of TolTEC's detector arrays are fabricated with a TiN/Ti/TiN trilayer on a single silicon-on-insulator wafer with integrated backshorts. The detector array wafers are aligned and mounted to an additional set of silicon wafers that make up a silicon-platelet feedhorn array and a waveguide coupling interface. Once together, the entire silicon structure is affixed to an OFHC copper housing via spring loaded mounts. A readout interface board carries the drive and signal lines to and from the detector array via wirebonded contacts and SMA connectors carry the signals to/from the copper mount (see lower-right photo in Figure 2).

The innermost assembly is thermally isolated and supported by five thin wall carbon fiber tubes attached to a copper structure at 1.2 K which also serves as a thermal break for the incoming and outgoing readout lines. A quasi-optical low-pass filter is mounted at the entrance aperture of the 1.2 K copper mount, directly in front

of the array of feedhorns. In order to mitigate stray light and blue-leaks, the side-walls of the 1.2 K mounting structure are taped with copper tape and carbon-infused cloth is strategically applied on internal surfaces to deaden the resulting cavity.

The outermost components of the array assembly are composed of an aluminum mounting structure which mechanically supports the 1.2 K assembly via six thin-wall carbon fiber tubes and a custom Amumetal A4K magnetic shield. For the 1.1mm array, a field-flattening silicon lens is mounted in the optical path at the front of the array assembly.

Once assembled on a lab bench, the array assemblies bolt directly to the optics bench and receive the respective stainless steel coaxial cables that carry the drive and sense signals for the detector networks. The set of low noise amplifiers (LNAs) that accompany each array are located physically close to the array assemblies to minimize loss in the transmission lines. The relative placement and orientation of the three array assemblies on the optics bench is shown in Figure 3.

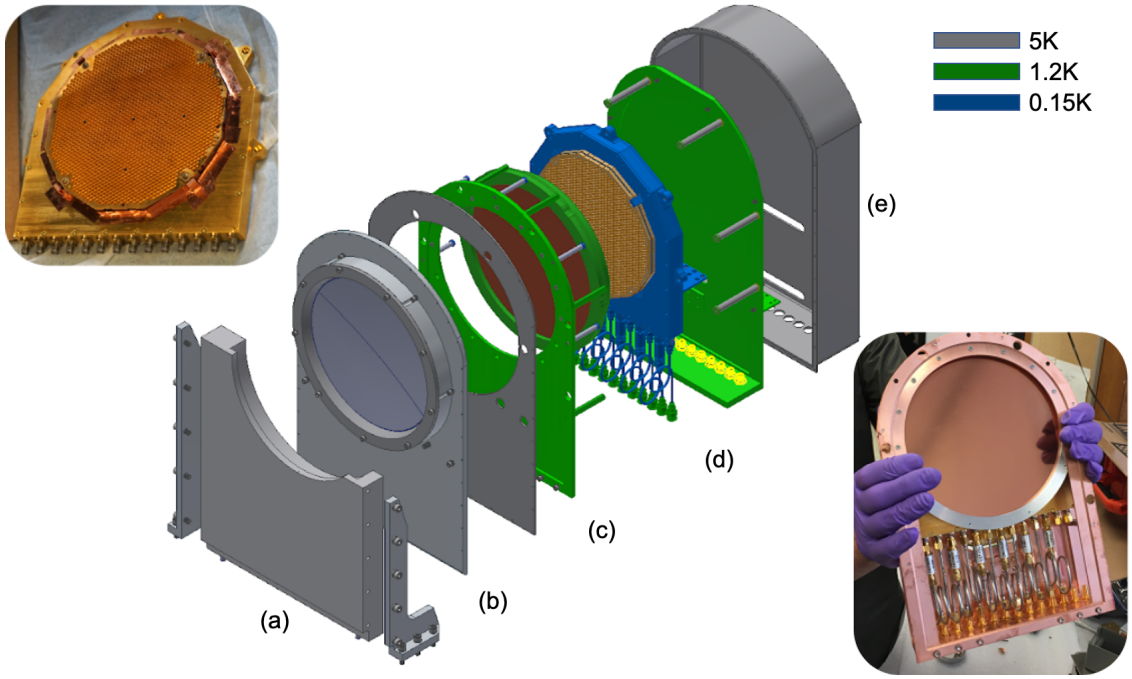

Figure 2. An exploded view of the 1.1 mm array detector assembly. The assembly is composed of: (a) an aluminum mount that bolts directly to the aluminum optics bench, (b) a silicon field-flattening lens, (c) a low-pass filter which serves as the aperture to an enclosed 1.2 K volume, (d) the silicon platelet feedhorns and detector array module at 0.15 K, and (e) a magnetic shield enclosure at 5 K. (Lower right:) A view of the 1.2 K and colder portions of the assembly showing the 14 stainless steel coaxial cables which carry the drive and sense signals to and from the array networks. These cables are hand-bent to provide the required thermal break between the 1.2 K and 0.15 K stages.

The detector signals are amplified prior to leaving the 4 K volume by custom-made low noise amplifiers (LNAs) operating in the 400-1200 MHz band.[7] These LNAs have 30 dB of gain with a noise temperature of 3.3 K in the band while dissipating less than 7 mW per amplifier. The LNAs are individually packaged to facilitate swapping or replacing, though we have not replaced the original set since initially installing them in 2019. The LNAs are powered via a pair of custom bias boards that are enclosed in RF tight packages on the two sides of the cryostat.

2.3 Optics

TolTEC's optics are described in a companion paper in these proceedings (**#11453-5**). Here we provide a general overview of the optics internal to the cryostat. Radiation enters the cryostat via a 330 mm diameter anti-reflection coated Ultra-High Molecular Weight Polyethylene window, following the design of the SPIDER

Project[8] where it immediately encounters a 300 K IR filter with a cutoff at 250 cm^{-1}. It then passes through a 45 K scattering filter at normal incidence followed by three 45 K IR filters, each angled at 8° with respect to the previous filter in the chain. The three IR filters have cutoffs at 250 cm^{-1}, 250 cm^{-1}, and 20 cm^{-1} respectively. Radiation surviving these filters then passes through a 4 K filter cartridge containing 2 IR blocking filters, each angled at 20° followed by a pair of low-pass filters with cutoffs of 16 cm^{-1} and 12 cm^{-1}. This final filter and its mount are located at an image of the primary mirror and so serves as the Lyot stop of the system. The window anti-reflection coating and all filters and dichroics in the optical system are provided by QMC Instruments in Cardiff, Wales.

Once through the Lyot stop, the radiation is inside of the 4 K volume which is enclosed by aluminum walls from above and an aluminum optics bench from below. A 0.75 m×1 m blackened copper sheet is mounted to the ceiling of the volume and thermally anchored to a 4 K bar to"deaden" the cavity. In addition, a 28.5 cm long baffle at the Lyot stop at 1.2 K provides additional baffling to any IR or scattered in-band radiation. The 4 K optics bench and its components are shown in Figure 3.

Light from the Lyot stop reflects off of a parabolic aluminum mirror and is focused and redirected onto a dichroic filter, D1 with a clear aperture of 278 mm. Radiation passing through D1 is refocused by a pair of silicon lenses before encountering a final low-pass filter at 10.3 cm^{-1} and being absorbed by the 1.1mm array. Radiation that reflects off of dichroic D1 is refocused by a silicon lens prior to encountering the second dichroic filter in the system, D2, which has a clear aperture of 225 mm. Light passing through D2 is again refocused by a silicon lens before passing through an 8.7 cm^{-1} low-pass filter and being absorbed in the 1.4mm array. Finally, light reflecting off of D2 is refocused by a silicon lens before passing through a 5.7 cm^{-1} low-pass filter and being absorbed by the 2.0mm array.

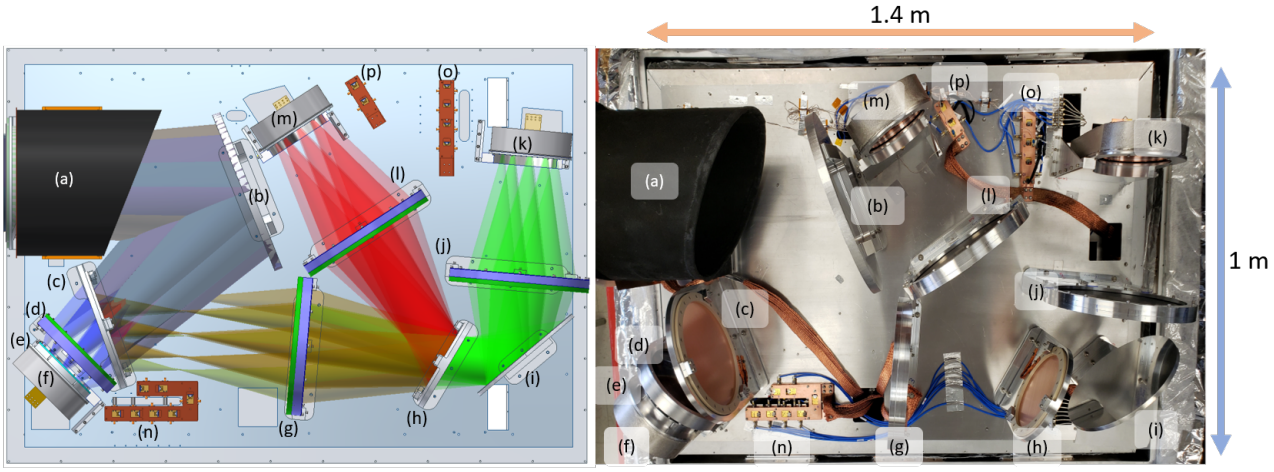

Figure 3. *Left*: Optics bench CAD model. The labels correspond to: (a) 1.2 K Lyot stop baffle, (b) parabolic mirror, (c) dichroic D1, (d) silicon lens 1, (e) silicon lens 2, (f) 1.1mm array, (g) silicon lens 3, (h) dichroic D2, (i) flat mirror, (j) silicon lens 4, (k) 1.4mm array, (l) silicon lens 5, (m) 2.0mm array, (n) LNAs for the 1.1mm array, (o) LNAs for the 1.4mm array, and (p) LNAs for the 2.0mm array. *Right*: Photo of optics bench with optics elements installed.

2.4 Half Wave Plate and Rotator

Ground-based observations at millimeter wavelengths must contend with atmospheric noise at low temporal frequencies. Though the atmosphere is unpolarized at these wavelengths, its total intensity is several orders of magnitude brighter than the astronomical signal. Each of TolTEC's detectors are sensitive to a single linear polarization of the incoming radiation and so the arrays are inherently capable of measuring polarization. For TolTEC's deepest polarization-sensitive observations, we will modulate the incoming polarized signals with a continuously rotating half wave plate (CRHWP). This is a common method of mitigating both atmosphere and low-frequency ($1/f$) noise.[9,10] By spinning the CRHWP at an appropriately high rate, the modulation shifts the polarized input signal to frequencies well above the $1/f$ noise in the atmosphere and detectors.

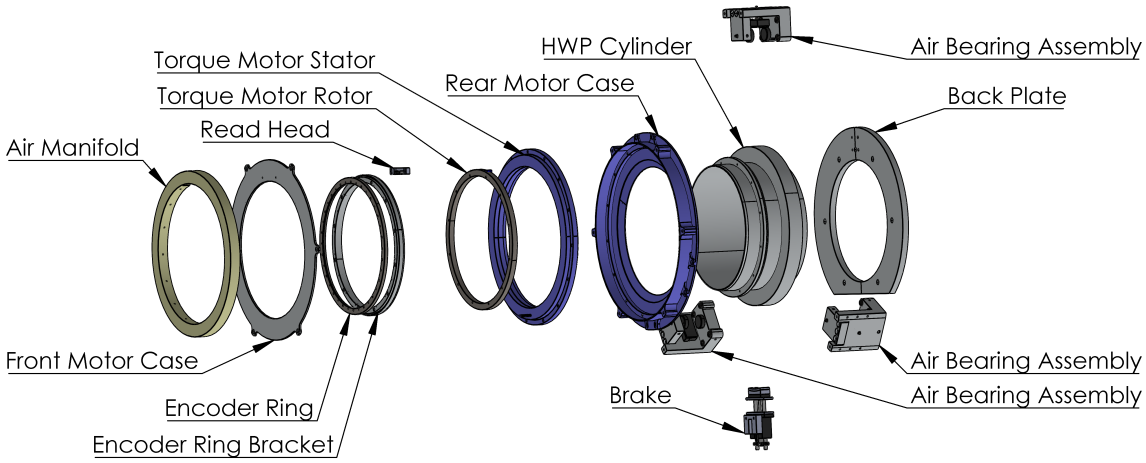

Figure 4. Exploded view of the half-wave plate rotator. (Minor accessories and components excluded.)

2.4.1 Half-Wave Plate Rotator

The half-wave plate rotator mechanism is designed to rotate a half-wave plate at a rate of 2 Hz which will push the polarized optical signal to 8 Hz in the detector time-streams. Mounted in front of the window into the cryostat, it modulates the signal prior to it entering the cryostat. The rotation of the half-wave plate (HWP) is achieved using three radial air bearings and six axial air bearings from New Way. Operating at 100 psi pressure, these air bearings provide low-friction and contactless rotation to minimize vibrations between the HWP rotator and the receiver to which it bolts. The rotation is driven by a commercial torque motor from Allied Motion. This choice of motor eliminates the need for a gear/belt system and thus, any associated mechanical vibrations.

A Renishaw high precision encoder ring is mounted on the rotor to mark the orientation of the rotor and HWP. The encoder ring consists of 65,536 lines distributed along the 417 mm diameter. Used in conjunction with a Renishaw VIONiC 4x interpolation optical read head, this system is capable of a resolution of ≈ 4.94 arcsec. A commercial off-the-shelf Sensoray S826 PCI Express I/O card is used to readout the encoder signal at a sample rate of 500 Hz. This information is then timestamped with a pulse-per-second signal shared between all TolTEC components before being sent to the data processing computer. An exploded view of the HWP rotator is shown in Figure 4.

2.4.2 Half-Wave Plates

Two separate achromatic HWPs will be used to rotate the linear polarization of the incoming signal; one optimized for the bands centered on 1.1 mm and 1.4 mm, and another optimized for the bands centered on 1.4 mm and 2 mm. These will be swapped depending on the scientific observations being made. Achromatic HWPs enable operation over a range of wavelengths.[11] While, in theory, one HWP could be used to span all three bands, our modeling shows that there is a trade-off between the extent of the usable bandwidth of the HWP and the degree of mismatch of the reflectivities and emissivities in the two orthogonal axes. Because our HWP is at room temperature, any mismatch in these quantities leads to a change in total optical loading on the detectors that shows up at $2\times$ the rotation frequency of the HWP. We have modeled the effect of this changing power on the detectors, which continuously changes the optimal readout frequency of the resonances, and have quantified the effective increase in system noise. We then carried out extensive modeling and simulation of potential HWP designs, and iterated through these models prior to manufacture. Our conclusion is that a single three-band HWP results in high performance compromises between the bands (i.e., reducing the HWP synchronous signal for one band inevitably increases it for at least one other band). We ultimately decided that two two-band HWPs would be the most conservative solution to this issue. Each HWP is designed to minimize the impact

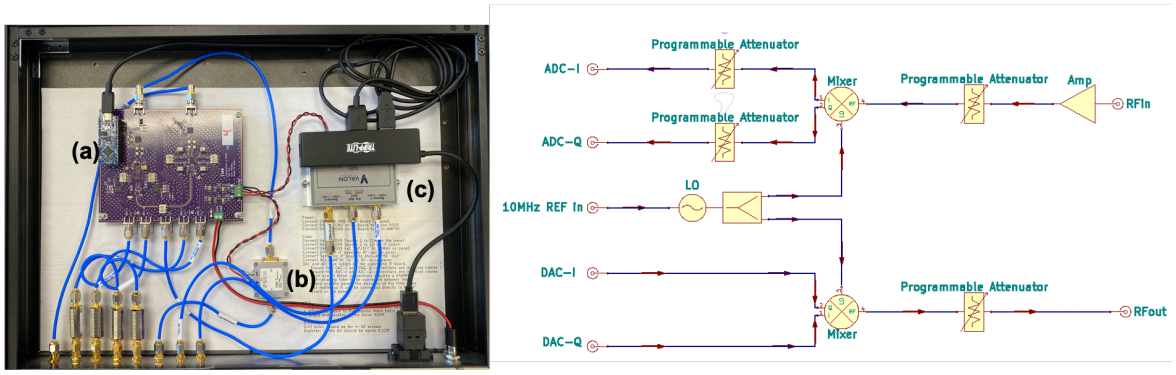

Figure 5. (Left:) Photo of the IF slice. Labeled components include (a) the new generation 3 custom circuit board, (b) the 30 dB input amplifier, and (c) a Valon 5009 IF synthesizer. (Right:) Block diagram of the generation 3 IF electronics. The system was significantly simplified and made more compact by moving several commercial components onto one custom printed circuit board.

of the HWP synchronous signal in both its respective bands, while still preserving the benefit and flexibility of multi-band observations. The HWPs can be easily swapped or even entirely removed if desired for total-intensity observations.

2.5 Readout Electronics

TolTEC's readout electronics were developed at ASU and were based on the heritage designs of the BLAST-TNG readout system.[12,13] We will focus on upgrades to that system for TolTEC here. The system consists of a set of thirteen 1U enclosures housing the ROACH2 and MUSIC readouts (called the digital slices and also used in the OLIMPO experiment[14]) paired with 13 additional 1U enclosures, each containing intermediate frequency (IF) electronics with a programmable RF front-end (called the IF slices). Each pair of slices produces a set of up to 1000 user-programmable probe tones that provide drive power and sensing signals for the resonators in a network over a 500 MHz RF bandwidth. For TolTEC the center of the probe tone band is approximately 700 MHz.

The RF performance requirements for the readout slices are the same for TolTEC as for BLAST-TNG but the environmental conditions in operation are significantly different. For BLAST-TNG, conduction based cooling via heat pipes were used which required a custom enclosure and large thermal mass. In addition, the RF front-end electronics were allotted a small volume on the gondola which made servicing difficult and risky. Learning from this, the TolTEC readout uses the stock fans installed for cooling with separate 1U enclosures for the ROACH2 and IF slices. The overall system takes up 30U of rack space - including power supplies and power distribution - to drive and read out 13 networks of detectors. The system is fully modular and swapping or replacing slices takes only a few minutes.

The RF front-end electronics went through three iterations of development. In an effort to reduce the size, optimize performance, and reduce cost, a set of custom integrated RF front-end boards were developed. The first generation utilized individually packaged components. The second generation implemented custom Arduino controlled programmable attenuators. The third generation, shown in Figure 5, integrated most components onto one board: the two mixers, multiple programmable attenuators, sense RF amplifiers, and baluns for differential to single-ended conversion. The receive chain was finalized after optimizing the signal to noise in loopback measurements. A loopback phase noise measurement of -100 dBc/Hz with a 1000 tone frequency comb is typical for generation 3. Detector phase noise levels are typically above -80 dBc/Hz. The image tone suppression, without digital correction, is -20 dB or better. To ensure that the incoming signals are well above the mixer noise floor, we added an amplifier with an output compression higher than the input compression of the demodulator.

Generation 3 also includes a local oscillator (LO) nulling as a new feature that had not been implemented in previous iterations of the IF system. The BLAST-TNG readout IF system often had LO leakage tone power over 5 dB higher than the detector probe tones. The detectors are very sensitive to the overall power sent through the array. Lowering the LO leakage from the IF electronics helps to prevent the situation where the detectors are being over driven. LO nulling helps to ensure that the dominant RF power is from the probe tones only.

2.6 Readout, Monitor and Control Software Architecture

Here we describe the flow of data from the readout electronics through the production of images and data products. Our readout and data collection system architecture is shown in Figure 6. TolTEC's 13 ROACH-2 readouts each stream data over point-to-point Ethernet connections to a CLIP computer, whose primary task is to write the data to disk, perform detector characterization analyses, and to send control signals to the ROACH-2 systems. A clip-manager computer, CLIPY, manages the overall system state and provides monitor and control software for the instrument team. By decoupling the management tasks from the data collection tasks, the data acquisition system is robust against asynchronous user interactions and is scalable to any size detector array.

In parallel with the primary data acquisition system, a timely analysis computer, TACO, acts as a real-time replica of all of the CLIP data in order to provide a primary location for general users and telescope operators to get quick-look data products and visualizations, and to easily monitor the system state. On TACO, an instance of the TolTEC analysis software, TolTECA (see below), continuously analyzes all incoming data. Data products are written both to disk and to a Redis database (in memory), which is monitored by a DASH-based service which serves as the front-end user interface. By separating the functionality of TACO from the primary data acquisition system, we have created an interface to the camera that buffers the data acquisition from asynchronous requests for data products from multiple users. In other words, users on TACO can not interfere with the data acquisition process.

The data analysis framework for the TolTEC project is called TolTECA. It includes all software required to get science-ready data products from the TolTEC instrument. While a detailed description of TolTECA will be presented in paper **#11452-110** in these proceedings, here we give a high-level overview of the structure of the codebase. The left panel of Figure 7 shows an overview of the architecture of TolTECA.

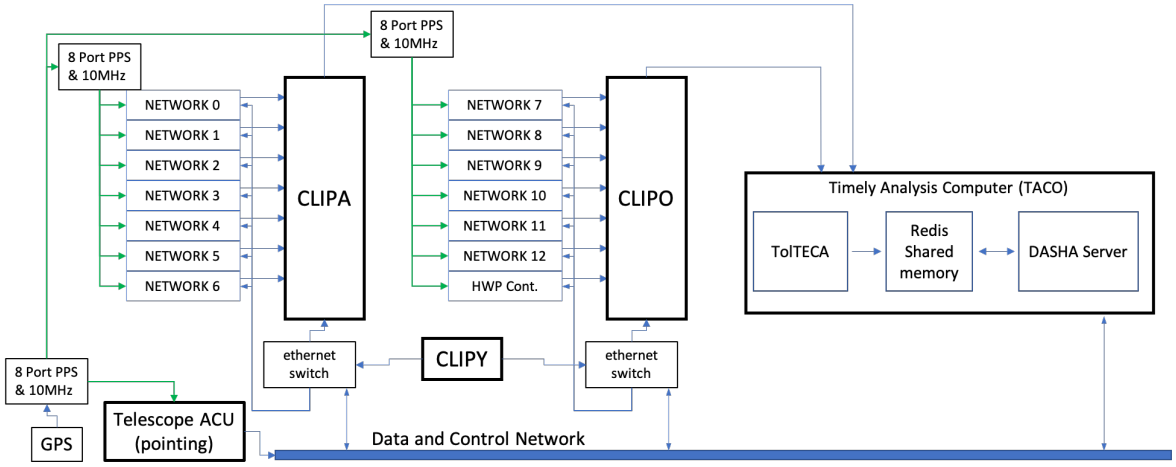

Figure 6. The TolTEC data handling hardware at the LMT site. Data is served by TolTEC's 13 Roach-2 systems (labeled as "Networks" here) and collected by two CLIP computers. The CLIPs are manged by the clip-manager, CLIPY. Data synchronization is achieved with a network of PPS generators with a common GPS-driven source. A specialized Timely Analysis Computer (TACO) acts as a real-time replica of all of the TolTEC data and provides quick-look analysis and instrument monitoring.

At the heart of TolTECA, the data reduction engine `citlali` is responsible for converting the recorded raw data to science-ready data products. An overview of the pipeline stages is shown in right panel of Figure 7. In brief, the pipeline starts with reading in the raw data files, which contain the multiplexed KIDs readout signals, and converts them to time-ordered data (TOD) that carries the optical power loading signals. The TOD are then filtered and down-sampled before they enter into the last stage, in which the final maps are made. For our in-lab testing, we exercise the `citlali` pipeline to reduce the Wyatt beam response testing data and the results are presented in § 3.2.5.

The various sub-modules of the Python package `tolteca` provide high level user interface and functionalities involved with processing the TolTEC data. `tolteca.web` is a quasi-real time, web-based data reduction and

visualization service that provides the observing-time diagnostics and user-feedback for telescope operators to execute successful and high-quality observations. `tolteca.simu` provides a TolTEC data simulator to help design, assess, and optimize the mapping strategies and to provide guidance to planning science programs. At the data centers where TolTEC data will be processed, all the data reduction tasks are executed by the `tolteca.pipeline`, and the created data products are managed by the `tolteca.datamodels`.

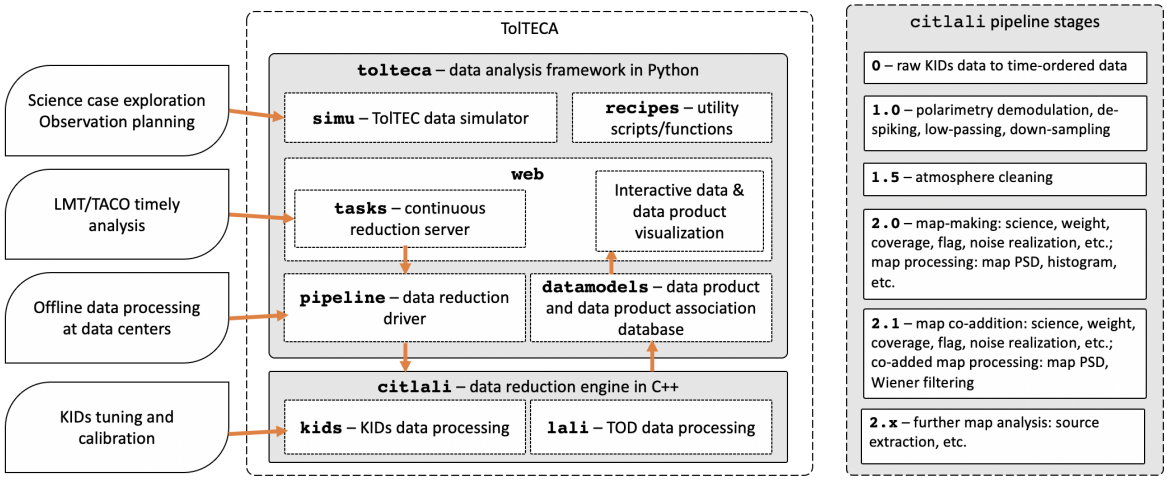

Figure 7. (Left:) The overall architecture of TolTECA. (Right:) The `citlali` data reduction pipeline stages.

3. IN-LAB SYSTEM CHARACTERIZATION

TolTEC has been fully integrated in the lab at UMass since late 2019 where we have been making measurements and continuously building new software tools for data visualizations and analysis. In this section we will walk through a number of the types of tests we use to characterize the system.

3.1 Detector Identification and Tuning

3.1.1 Detector Identification Sweeps

The TolTEC readout electronics use a microwave multiplexing approach that supports up to 1000 detectors on each readout circuit (i.e., maximum 1000 readout channels), which we refer to as a "network." In all, TolTEC's arrays require 13 networks: 7 for the 1.1mm array, 4 for the 1.4mm array, and 2 for the 2.0mm array. Once the cryostat is cold and the arrays have thermalized, we identify the detectors in each network by building a waveform of 1000 equally spaced readout tones, spanning the 500 MHz of readout bandwidth, and then sweeping each network's local oscillator (LO) over a range of 1 MHz in steps of 2 kHz. This fully samples the readout bandwidth with each frequency bin being sampled by two different readout tones at two different times in the sweep. The entire sweep takes 24 s.

An example sweep is shown in Figure 8. If the detectors all occupy unique positions in the network's bandwidth, finding the resonators would be fairly easy. This is not the case due to stochastic errors in the fabrication and so some fraction ($\sim$5%) of the resonators overlap and are blended. Moreover, the per-channel readout signals, S_{21}, are subject to the different gains of the individual channels, which gives rise to a varying baseline and discontinuities at the edge of each section of the sweep. This makes reliable and consistent identification of the individual resonator responses difficult. To improve the identification of the detectors we calculate the derivative of the S_{21} readout with respect to frequency, $\frac{\mathrm{d}S_{21}}{\mathrm{d}\nu}$, and iteratively fit and subtract our resonator model until the residuals are consistent with noise. With this approach we typically recover 96% of the resonators known to be in the network from fabrication. Table 1 lists the 13 networks and the total numbers of KIDs reliably identified in each one.

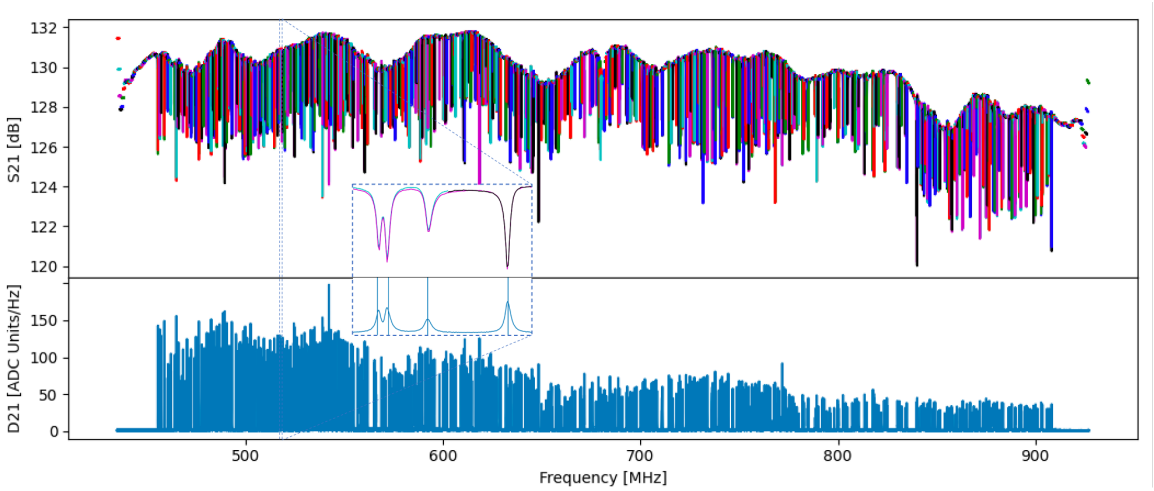

Figure 8. A typical network sweep showing the full 500 MHz bandwidth of the readout. The inset shows an approximately 1 MHz portion of the network containing a blended pair of resonators and two unique resonators. This sweep identified 643 of the 663 resonators identified by eye in this network, which was designed to have 684 resonators - for a total yield of 94%.

3.1.2 Tune Procedure

Once detectors are identified in the detector identification sweeps, individual readout tones are placed at the frequency of each resonator as determined by the finding algorithm. There is no electrothermal feedback in a KID readout and so as the optical loading on the detectors change, we must periodically "tune" the readout tones back onto the resonators. We do this with a series of "target" sweeps - one to identify the optimal locations in frequency for the readout tones, and another to verify the choice. Each target sweep is performed by sweeping the LO by ±87.5 kHz in steps of 1 kHz. The I-Q data for each detector from the first target sweep is fit to a generic KID resonator model of the form

$$S_{21}(f_p) = \mathcal{G}(\tilde{S}_{21}(f_p; f_r, Q_r))\,, \tag{1}$$

where $\tilde{S}_{21}$ is introduced as the "canonical" form of the transmission coefficient, expressed as

$$\tilde{S}_{21} = \frac{Q_r}{1 + 2\mathrm{i}Q_r \frac{f_p - f_r}{f_r}}\,. \tag{2}$$

Array	Network	Design	by-eye	Automated
1.1mm	0	684	663	643
	1	522	511	494
	2	558	551	552
	3	564	561	556
	4	556	551	557
	5	510	501	502
	6	618	607	590
1.4mm	7	676	662	652
	8	588	561	567
	9	590	580	601
	10	678	639	609
2.0mm	11	544	533	526
	12	628	594	588

Table 1. An accounting of the resonators in the three TolTEC arrays by design, identified by eye, and identified with our automated approach. In all, the automated approach reliably identifies 96% of the resonators.

Introducing

$$r \equiv \frac{1}{2Q_r} \tag{3}$$

$$x \equiv \frac{f_p - f_r}{f_r} \tag{4}$$

$$X \equiv r + x\mathrm{i}\,, \tag{5}$$

Equation 2 can be rewritten to a more symmetrical form

$$\tilde{S}_{21} = X^{-1}\,. \tag{6}$$

The function $\mathcal{G}$ in Equation 1 is related to the complex gain of readout circuit and is parameterized as

$$\mathcal{G}(\tilde{S}_{21}; G, K, M) = G\tilde{S}_{21} + Kf + M \tag{7}$$

where G, K and M are complex parameters.

From the fitting, we obtain the best model parameters f_r, Q_r, G, K and M. We use the set of fitted f_r as the refined locations of the tone lookup table, and a second target sweep is made to verify the results. This entire tuning process takes 34s in total.

Figure 9 shows a typical model fit in the I-Q plane with the $\tilde{S}_{21}$ (i.e., "normalized" to remove the gain signature) data and model. Following Equation 6, we use the fitted parameters from each tuning of the arrays to transform timestream (I, Q) data to timestream (r, x) channels, where x-values are proportional to the optical power variations on the detector and r-values are a quadrature channel sensitive to the readout noise.

We monitor the quality of the tuning of each resonator by measuring the angle, $\phi \equiv \arctan(-x/r) = \arctan(\tilde{Q}/\tilde{I})$. Perfectly in-tune resonators have $\phi = 0$. Our resonator model allows us to predict the readout noise degradation as the resonator goes out of tune and so we monitor the set of θs for the system so that we may run the tuning procedure when needed. The readout noise degradation can be expressed as a function of ϕ, or equivalently the central angle $\theta \equiv 2\phi$, as shown in Figure 9. Ultimately, the allowable range of θ will be determined by the extent to which the system is background limited.

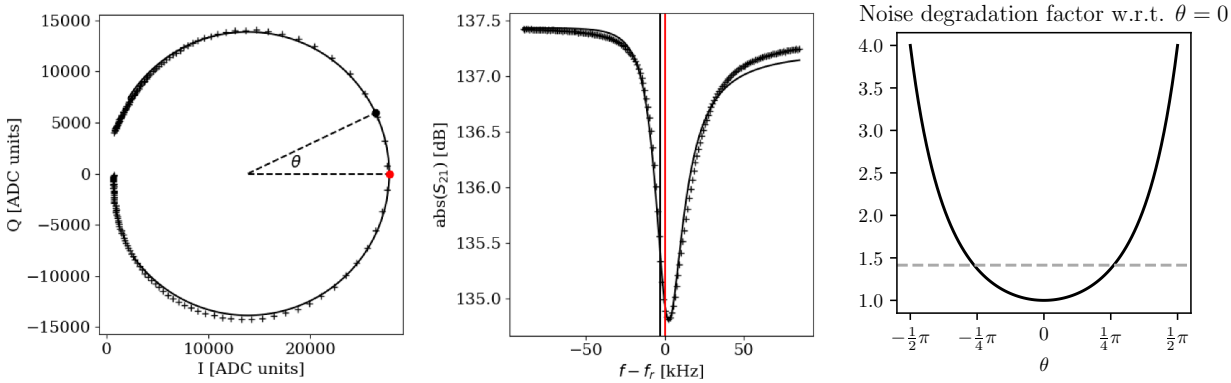

Figure 9. (Left:) A typical resonator I-Q plane data and model. The red dot signifies the optimal tone location while the black dot shows the current tone location prior to the tuning. (Middle:) The same data as in the left figure but in the frequency-S_{21} plane. As described in the text, the model is weighted to match the data in the resonance rather than in the wings. The vertical lines show the optimal tone location (red) and current tone location (black). (Right:) The noise degradation as a function of detuning, θ for this detector. The horizontal line marks the angles where the readout noise is $\sqrt{2}$ greater than when the resonance is optimally tuned.

3.1.3 AutoDrive

Every KID in the system has a *unique* tone probe drive power that will result in the lowest readout noise for that detector. We have developed an automated procedure for finding these powers (or drive tone amplitudes) empirically by systematically performing target sweeps from low to high drive power and determining, for each resonator, what drive power results in a bifurcation of the resonance. This procedure naturally accounts for varying transmission across the network bandwidth (see Figure 8) and the varying physical parameters of different detectors.

We determine the best drive power for a resonator by quantifying the degree of bifurcation of the resonator from the target sweep data as a function of the driving power. In brief, we rely on the notion that an optimally driven detector yields a smooth, symmetrical $D_{21} \equiv \left\| \frac{\mathrm{d}}{\mathrm{d}f} S_{21} \right\|$ profile that reads

$$D_{21} = \frac{2\|G\|}{f_r} \left\| \tilde{S}_{21} \right\|^2, \tag{8}$$

which peaks at the resonance frequency f_r. Three observables can be used to identify when a resonator bifurcates: 1) the D_{21} profile becomes asymmetric, 2) the peak value of D_{21} becomes offset from the resonance frequency, and 3) the peak value of D_{21} dramatically rises. These three features are illustrated in the left panel of Figure 10. We currently use the third of these observables to determine the optimal drive power. Using data from the target sweeps at different drive powers, for each detector we identify the drive power where the D_{21} peak value is 1.2 times the peak value at low drive power as shown in the right panel of Figure 10. While the choice of 1.2 is somewhat arbitrary, we have empirically found this to result in good detector performance across each network.

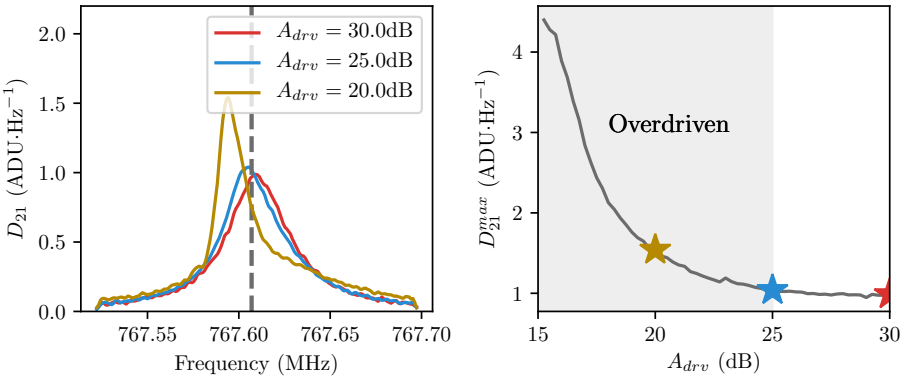

Figure 10. (Left:) A plot of the D_{21} profiles of a detector driven with different drive powers spanning the point of bifurcation. (Right:) The peak value of D_{21} as a function of the driving power. The detector is considered over-driven, or bifurcated, in the shaded region. We choose the optimal drive power to be that where D_{21}^{max} is larger than 1.2× the mean value of D_{21}^{max} at lower drive powers.

The result of the AutoDrive procedure is a list of optimized input tone powers that maximally drive the detectors before they are over-driven. A comparison of the detector responses before and after the AutoDrive is shown in Figure 11. With the AutoDrive applied, we can see that for a large number of detectors the readout signal (as indicated by the D_{21} peak) is maximized with no detectors being bifurcated.

3.2 In-lab Optical Measurements

We have performed a series of in-lab optical characterizations of the system over the past two years. In all of the cases below, a 7.5 K blackened plate was placed at the input Lyot stop - just inward of the 4 K IR and low-pass filters at the optical entrance of the 4 K volume. The plate has, at its center, a 25 mm diameter aperture that allows 0.45% of the detectors' etendue to pass through to the room. Approximately 35% of the detector etendue intercepts the 7.5 K blackened plate while the remainder is intercepted either by the surrounding 1.2 K blackened baffle or some other surface in the cold volume.

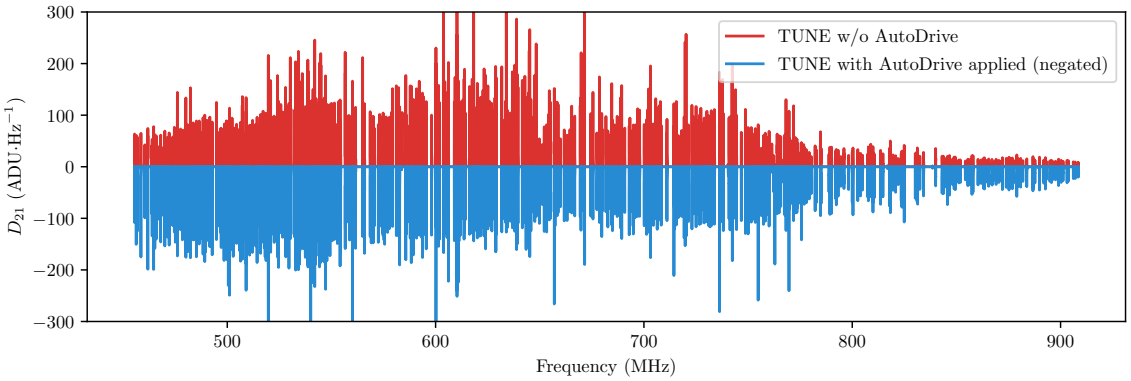

Figure 11. A comparison of the sweep $\|D_{21}\|$ spectra, with and without the AutoDrive correction applied (the blue is plotted negated for visualization purposes). With AutoDrive applied, we see the readout signals are much more uniform across the entire frequency range. In particular, the peaks of the tones are much larger (resulting in higher signal-to-noise) for those at the high frequency end of the network.

During the optical tests in the spring of 2020 we discovered that the dichroic filters, which are flat at room temperature, bow with a radius of curvature of approximately 2 m at cryogenic temperatures. Optical tests of the 1.1mm array show that the effect of this bow is negligible when the dichroic is viewed in transmission. However the 1.4mm array views dichroic D1 in reflection and its optical response, as shown in some tests below, is adversely affected. The 2.0mm array views both dichroics in reflection and is even more adversely affected. We confirmed that the dichroics were the problem by swapping dichroic D1 with a flat mirror and repeating the optical tests. With the flat in place, the 1.4mm array's efficiencies (see Section 3.2.4) and beammap results (see Section 3.2.5) were as-expected while the 2.0mm array's values remained aberrant. With this information in hand, along with a careful study of the fabrication process of the dichroics, we now believe we understand the root cause of the issue. A new dichroic D1 was produced at Cardiff and is now installed and cooling in the camera at the time of this writing.

3.2.1 Cryostat Radiative Background

The overall size of the TolTEC cryostat and limitations of our high conductivity cooling straps leaves the possibility that there are hot spots inside the 4 K volume which could lead to a significant, unexpected optical loading on the detectors or filters. We have tested for this by constructing a macroscopic bolometer - a blackened 12 cm polypropylene octagon suspended by four 0.38 mm diameter nylon supports, each with a length of 10 cm. The heat transfer in this geometry is radiation-dominated at all of the optics bench's temperatures. A calibrated Cernox thermometer is mounted to the center of the absorber to track the bolometer's temperature both during cooldown and throughout our testing. This is the first time we have attempted to carefully measure the full bolometric radiation environment of the cryostat.

Data from our September 2020 cooldown show that the background radiation loading in the system takes approximately 1 week to settle after the optics bench reaches its base temperature. We have not identified which aspect of the system drives the long time constant. The lowest temperature recorded by the bolometer during the cooldown was 5.75 K though we note that the bolometer's temperature was still falling at a rate of ~ 0.25 K/day when the testing ended. We conclude that in this configuration there is no substantial and unexpected IR source in the cryostat. We will perform this test again, with the Lyot stop fully open to the 300 K room, before shipping to the LMT.

3.2.2 Spectral Measurements

We use a Fourier Transform Spectrometer (FTS) in the UMass lab to measure the passbands of each array. The FTS samples a relatively small fraction of the field of view of the arrays and so we sample the passbands by physically moving the FTS in front of TolTEC. The variations we see in this manner are small compared to the structure in the bands. Figure 12 shows the bandpass response of the three arrays along with our original

models of the optical design. Since our FTS works to THz frequencies, we have confirmed that no first or second harmonic filter response is detectable.

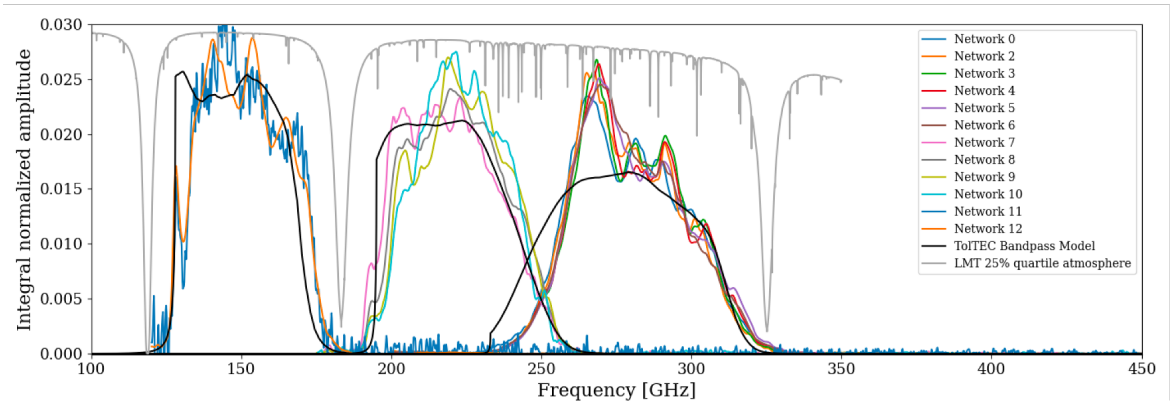

Figure 12. In-lab FTS measurements of the three TolTEC arrays. Each plotted curve is an average spectrum for the detectors in the respective network and has been normalized so that its integral over the passband is 1. The black curve in each case is the model spectrum originally predicted from the model filter response functions. The light grey line shows a scaled version of the atmospheric transmission at the LMT for opacity, $\tau_{225\mathrm{GHz}} = 0.1$.

3.2.3 Responsivity Measurements

The responsivity, S, of our KIDs is the change in the detuning parameter, x, with changing optical load, or $\frac{\mathrm{d}x}{\mathrm{d}P_{opt}}$. We can not easily measure this, but we can measure a very similar quantity which is the change in resonant frequency with changing optical load. The two are related by:

$$S = \frac{\mathrm{d}x}{\mathrm{d}P_{opt}} = \frac{f_r}{f_p}\frac{\mathrm{d}f_r}{\mathrm{d}P_{opt}} \approx \frac{\mathrm{d}f_r}{\mathrm{d}P_{opt}}. \tag{9}$$

where f_r is the resonant frequency and f_p is the probe frequency, which are typically the same to better than one part in 10^4. To measure the change in resonant frequency with input optical power we place a custom-built cryogenic blackbody on the TolTEC optics bench directly in front of the detector arrays to intercept the detector response as close to the feedhorn apertures as possible. In practice this distance was approximately 10 cm. The blackbody was made from TK THZ RAM Tiles* mounted to a copper plate that was stood off from the optics bench by a set of G-10 standoffs. A series of aluminum foil straps were used to set the time constant of the suspended structure to approximately 1 hour. A photo of the setup is shown in Figure 13.

The measurement is then as follows. With the blackbody heater off and the blackbody as cool as possible (typically 5.5 K), we follow the tune procedure of Section 3.1.2 to determine the resonant frequencies of the detectors. In a step-wise fashion, we then heat the blackbody to 15 K, with a settling duration of 4 hours for each step. At each temperature, we again repeat the tuning procedure to find the new resonant frequencies. Figure 13 shows histogrammed results for networks in the 1.1 mm array and the 2.0 mm array. We did not do this test for the 1.4 mm array since the measured responsivities for the other arrays were very close to the design values. The responsivities of the two arrays are intentionally different in order to equalize their readout noise under their different expected optical power loading.

3.2.4 Efficiency Measurements

We measure the optical efficiency of TolTEC's internal optics by comparing the resonant frequencies of the detectors when illuminated by 300 K and 77 K beam filling loads placed at the cryostat window and viewed by the detectors through the Lyot stop aperture. The aperture, which is only present for in-lab optical measurements, passes 0.45% of the detector etendue. Figure 14 shows histograms of detector efficiencies for the three different

*Thomas Keating Ltd., www.terahertz.co.uk

arrays under two different setup configurations. The 1.1mm array efficiencies are measured with the standard optics configuration shown in Figure 3 above. These match the expected distribution (shaded region) well. The middle and right panels of Figure 14 show the 1.4mm and 2.0mm array efficiencies when dichroic D1 is replaced with a flat mirror. The 2.0mm array efficiencies remain low presumably because this array must view the source in reflection off of dichroic D2, which is still in place in this setup.

3.2.5 Lab Beam Response Testing

We performed a check of the internal optical systems of the cryostat using a Hawkeye Technologies IR-75 Source operating at 973.15 K whose output is modulated at 10 Hz. Our goal in these in-lab tests was to verify the common focus of the three detector arrays, verify a common alignment of the three detector arrays, and spatially identify each detector in the arrays with their corresponding resonant frequency and network. Since we don't

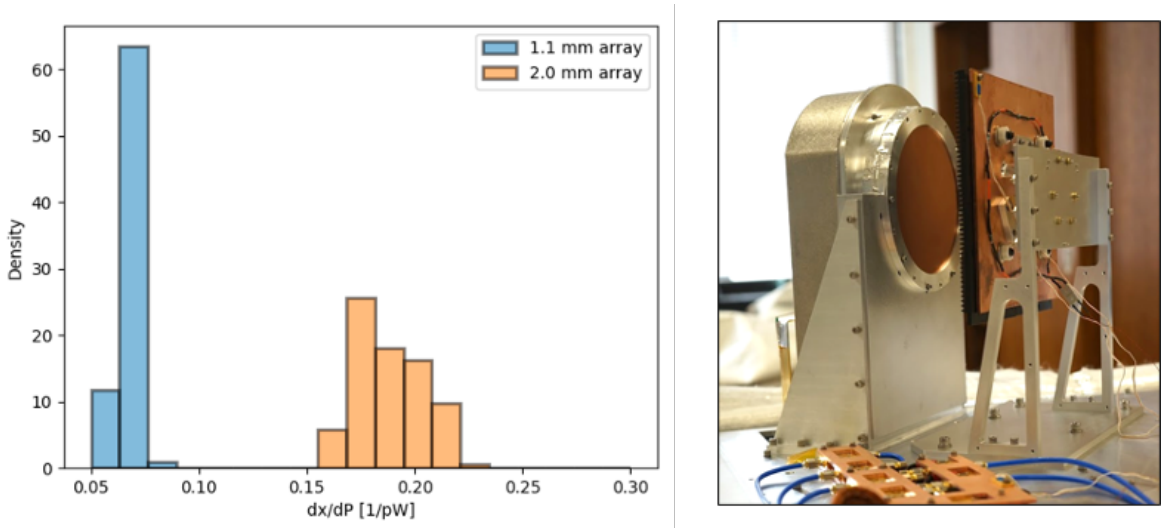

Figure 13. (Left:) Measured responsivity density histograms for networks 0, 2, and 4 from the 1.1mm array and networks 11, and 12 from the 2.0mm array. (Right:) The cryogenic blackbody mounted in front of the 2.0 mm array on the TolTEC optics bench. The blackbody temperature is controllable between 5 K and 15 K - the upper limit being where the blackbody starts to put a significant load on the 4 K stage of the cryostat.

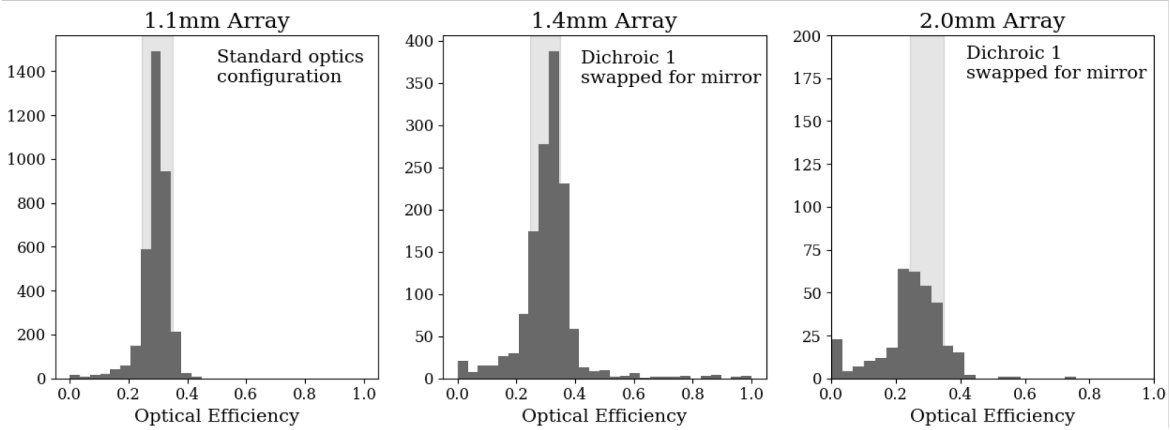

Figure 14. Measured optical efficiencies from the three arrays under the optical configurations described in the text. The shaded regions represent our expected efficiencies with 35% Lyot stop illumation efficiency and a detector coupling efficiency from 70% (lower end of the shading) to 100% (upper end of the shaded region). The 2.0mm array suffers from the effects of the bowed dichroic D2.

know the in-band brightness of the IR-75 source at millimeter wavelengths, we can not use these measurements as any sort of absolute calibration.

The IR-75 source is mounted on a 2 degree-of-freedom robot arm built using 12.5 mm diameter carbon fiber rods in a planar configuration. The positioning system, which we refer to as Wyatt, allows a circular workspace of just over 2 meters in diameter as shown in Figure 15. The shoulder joint is counter-weighted and direct-driven using a NEMA 23 servo motor. The elbow joint is driven using a toothed belt with a 1:1 ratio using a second NEMA 23 servo motor. In operation, the source is moved point-to-point along its trajectory and then holds its position for each measurement for a specified period of time. We measure the RMS of the relative positional accuracy of this system to be 2 mm and we define the position tolerance to be 10 mm, which are both better than we need for our optical measurements. Wyatt's control is tightly integrated into TolTEC's control system so that the data taking can be time-synchronized with the robot's actions.

The Wyatt system and source operate within a black carbon-enfused cloth enclosure, as shown in Figure 15, in order to minimize stray light and reflections. In a single observation, Wyatt is servoed to different positions in a user-defined grid in front of the cryostat window. The source is then integrated for 15 seconds before moving to the next position. The detector time streams are converted into the map domain by taking each 15 second integration period and calculating the power spectral density (PSD). The S/N is calculated in reference to the PSD calculated in a window adjacent to that containing the source modulation frequency. In this manner we generate a separate map of S/N over the grid of observations for every identified detector resonance. The source in each map is then fitted to a two-dimensional Gaussian. Over the course of a single night, several individual beammaping observations are taken and the beammaps for each array are coadded to improve S/N and the fitted centroid positions of the detectors. Figure 16 shows the positions of the detectors for each of the three different arrays.

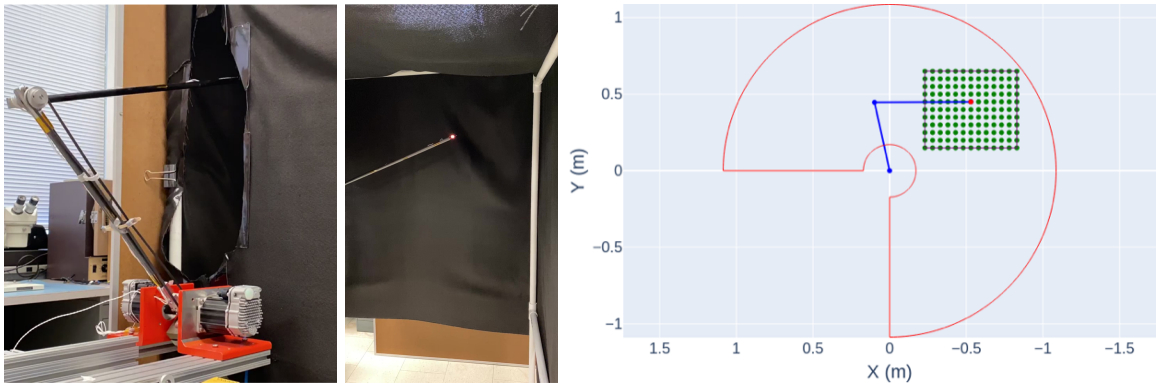

Figure 15. (Left:) A photo taken from the side of the IR-75 source mounted on the Wyatt robot arm inside of the carbon-enfused cloth enclosure. (Middle:) Front-view of the the IR source at the end of the robot arm within the enclosure. (Right:) Example of the grid of positions (green points) at which the robot arm (blue line) will stop to observe. Here, the points of the 11 x 13 grid are separated by 5.0 cm, giving an overall physical map scale of 50.0 x 60.0 cm. The area within red curve is the region that the robot arm is capable of moving to.

Early in-lab beammaps of the system revealed a problem associated with the 1.4mm and 2.0mm arrays. While the 1.1mm array maps matched our optical model well, the field of view and overall map qualities of the other two arrays did not. Over a series of tests and analyses throughout most of 2020, we traced this issue to a bow in the two dichroic filters with an approximate radius of curvature of 2 m. After confirming that this is not likely due to differential thermal contraction of the PEEK dichroic mounts and the polypropylene filters, we now suspect that the bow is the result of a specific filter manufacturing process step. As of this writing, our collaborators at Cardiff have produced a new Dichroic 1 using a different approach. We are cooling the cryostat with this new filter installed now with optical testing planned for the first week of December, 2020.

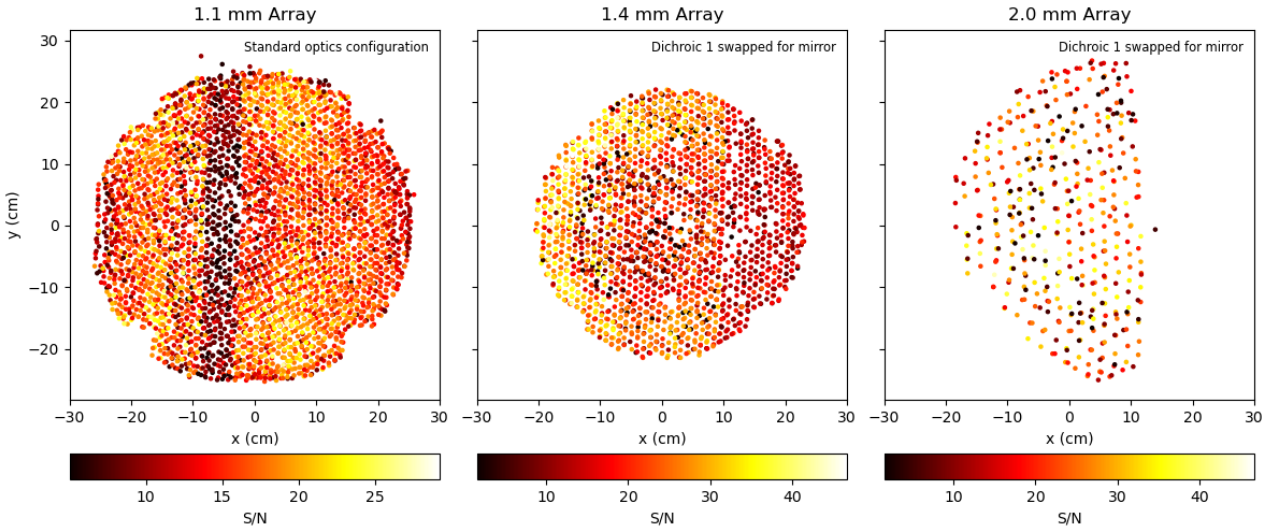

Figure 16. Scatter plots of the fitted x and y positions of each detector for all 3 arrays from the beammapping observations. The color scale is the fitted S/N of the source in the beammaps. Sources with S/N lower than 5.0, 1.4, and 1.0 have been removed for the 1.1, 1.4, and 2.0 mm arrays to exclude spurious detections. Only one of the two networks is plotted for the 2.0 mm array due to a wiring issue during that cooldown.

3.3 Noise Measurements

A full discussion of the noise properties of the TolTEC detectors will be the subject of a future paper. Here we describe the measured noise of the detector networks in the same optical configuration as the optical tests above, but with a shiny bowl-shaped reflector placed over the cryostat window. This configuration should closely replicate the optical loading with the lyot stop fully closed, which is considerably less than the loading expected at the LMT. Figure 17 shows a typical network's response. In the figure, the quadrature channel, r is sensitive to the readout noise and other non-optical noise sources in the system. The optically-sensitive channel, x, is sensitive to the same noise sources along with detector noise and any optically induced noise terms. For the detectors shown, the responsivity is 6.9×10^7 Hz/W. We use this value to scale the expected background limited photon noise (BLIP) from both the cryostat (5.5 K, see Section 3.2.1) and from the LMT.[3]

Figure 17 shows good agreement between the median detector power spectral densities (PSD) in the r and x channels given the expected BLIP from the cryostat. Moreover, the white portion of the median readout noise (above 1 Hz) is 6 times lower than the expected BLIP at the LMT in this measurement. We note that the noise is strongly dependent on the drive power and, more weakly, dependent on the effective Q_r of the devices.

Both the r and x channels show significant $1/f$ noise behavior at low frequencies. A principal component analysis shows that the $1/f$ is mostly common-mode in the r channel, but almost entirely independent amongst the detectors in the x channel. This is consistent with measurements made by the NIST team of other Ti/TiN/Ti devices. The same group has recently shown that Aluminum KIDS made in a similar dual-polarization scheme have much better $1/f$ performance.[15] For TolTEC, the atmospheric contamination also has a $1/f$ signature and so we expect these low frequency modes to be down-weighted in our mapmaking algorithm. The spinning half-wave plate modulator will boost polarized signals to 8 Hz and above and so should be further into the flat part of the detector PSD.

4. CONCLUSION

The TolTEC camera is nearing completion and deployment to the Large Millimeter Telescope. We have performed several in-lab characterization measurements and tests that show that the system has a high detector yield, a low background optical load, and low readout noise. Measurements with a Fourier Transform Spectrometer show that the three array passbands are in-line with our original models and that there are no measurable harmonic or

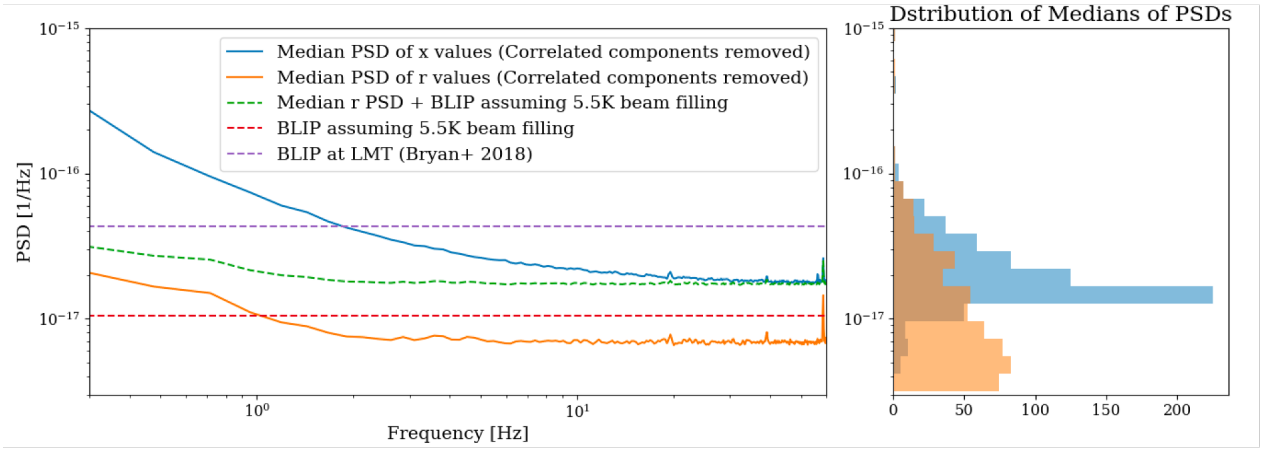

Figure 17. (Left:) Noise spectrum from a typical TolTEC network. The blue curve shows the median PSD of the optically active channels, x, which includes the effects of readout noise, detector noise, and background limited photon noise (BLIP). The orange curve is the median PSD of the quadrature channel, r which is sensitive to just the readout noise. In these units the median readout channel is approximately 6-times smaller than the median optical channel. The green curve is the PSD resulting from adding the expected 5.5 K cryostat background radiation noise (red dashed line) to the readout channel. The purple dashed line marks the expected background limited noise at the LMT. (Right:) The distribution of medians of the PSDs (the white noise level) of the 643 detectors in this network.

blue-leaks. The individual detector properties match our models and we have developed automated approaches to read-out the detectors and find their optimal bias points.

Optical measurements showed that our two dichroic filters suffer from bowing when cooled to cryogenic temperatures. A series of tests with different configurations, along with a careful study of the materials and manufacturing process, lead us to believe that the problem is inherent to the manufacturing process. We have adjusted the process and are now cooling the system with a new dichroic, D1, to confirm that this solves the problem.

The detector and system noise properties have been characterized under low-loading conditions. The readout electronics noise is sufficiently low to ensure background-limited performance at the LMT site. The detector noise levels should be consistent with background-limited performance at readout frequencies above a few Hz in unpolarized measurements and at nearly all frequencies when doing polarization measurements with the spinning half-wave plate.

The TolTEC system architecture is robust and convenient for setup and testing. The cryogenic system is sound and achieves stable base temperatures that should last for months at a time. The optical bench approach allows for rapid turn-around of the system and convenient access to the key elements. The software and readout system supports fully remote use of the camera.

ACKNOWLEDGMENTS

This work is supported in-part by the National Science Foundation, grant #1636621. The Mexican collaborators on TolTEC acknowledge support by Conacyt project FDC2016-1848. We also thank the Northwestern University Research Shop for their assistance with the design and construction of the Half-wave Plate Rotator and Tom Scott in the UMass Astronomy machine shop for machining a significant number of parts for TolTEC.

REFERENCES

[1] Hughes, D. H., Jáuregui Correa, J.-C., Schloerb, F. P., Erickson, N., Romero, J. G., Heyer, M., Reynoso, D. H., Narayanan, G., Perez-Grovas, A. S., Souccar, K., Wilson, G., and Yun, M., "The Large Millimeter Telescope," in [*Ground-based and Airborne Telescopes III*], Stepp, L. M., Gilmozzi, R., and Hall, H. J., eds., *Society of Photo-Optical Instrumentation Engineers (SPIE) Conference Series* **7733**, 773312 (July 2010).

[2] Montaña, A., Chávez Dagostino, M., Aretxaga, I., Novak, G., Pope, A., Wilson, G., and TolTEC Team, "TolTEC: unveiling the hidden universe.," *Memorie della Societa Astronomica Italiana* **90**, 632 (Jan. 2019).

[3] Bryan, S., Austermann, J., Ferrusca, D., Mauskopf, P., McMahon, J., Montaña, A., Simon, S., Novak, G., Sánchez-Argüelles, D., and Wilson, G., "Optical design of the TolTEC millimeter-wave camera," in [*Millimeter, Submillimeter, and Far-Infrared Detectors and Instrumentation for Astronomy IX*], Zmuidzinas, J. and Gao, J.-R., eds., *Society of Photo-Optical Instrumentation Engineers (SPIE) Conference Series* **10708**, 107080J (July 2018).

[4] DeNigris, N. S., Wilson, G. W., Eiben, M. E., Lunde, E., Mauskopf, P., and Contente, R., "Developing a Large-Scale Cryogenic System for the Simultaneous Operation of Three Detector Focal Planes in TolTEC, A New Multichroic Imaging Polarimeter," *Journal of Low Temperature Physics* **199**, 789–797 (Jan. 2020).

[5] Day, P. K., LeDuc, H. G., Mazin, B. A., Vayonakis, A., and Zmuidzinas, J., "A broadband superconducting detector suitable for use in large arrays," *Nature* **425**, 817–821 (Oct. 2003).

[6] Austermann, J. E., Beall, J. A., Bryan, S. A., Dober, B., Gao, J., Hilton, G., Hubmayr, J., Mauskopf, P., McKenney, C. M., Simon, S. M., Ullom, J. N., Vissers, M. R., and Wilson, G. W., "Millimeter-Wave Polarimeters Using Kinetic Inductance Detectors for TolTEC and Beyond," *Journal of Low Temperature Physics* **193**, 120–127 (Nov. 2018).

[7] Hosseini, M., Wong, W., and Bardin, J. C., "A 0.4–1.2 ghz sige cryogenic lna for readout of mkid arrays," in [*2019 IEEE MTT-S International Microwave Symposium (IMS)*], 164–167 (2019).

[8] Rahlin, A. S., Ade, P. A. R., Amiri, M., Benton, S. J., Bock, J. J., Bond, J. R., Bryan, S. A., Chiang, H. C., Contaldi, C. R., Crill, B. P., Doré, O., Farhang, M., Filippini, J. P., Fissel, L. M., Fraisse, A. A., Gambrel, A. E., Gand ilo, N. N., Golwala, S., Gudmundsson, J. E., Halpern, M., Hasselfield, M. F., Hilton, G., Holmes, W. A., Hristov, V. V., Irwin, K. D., Jones, W. C., Kermish, Z. D., Kuo, C. L., MacTavish, C. J., Mason, P. V., Megerian, K., Moncelsi, L., Morford, T. A., Nagy, J. M., Netterfield, C. B., O'Brient, R., Reintsema, C., Ruhl, J. E., Runyan, M. C., Shariff, J. A., Soler, J. D., Trangsrud, A., Tucker, C., Tucker, R. S., Turner, A. D., Weber, A. C., Wiebe, D. V., and Young, E. Y., "Pre-flight integration and characterization of the SPIDER balloon-borne telescope," in [*Millimeter, Submillimeter, and Far-Infrared Detectors and Instrumentation for Astronomy VII*], Holland, W. S. and Zmuidzinas, J., eds., *Society of Photo-Optical Instrumentation Engineers (SPIE) Conference Series* **9153**, 915313 (July 2014).

[9] Essinger-Hileman, T., Kusaka, A., Appel, J. W., Choi, S. K., Crowley, K., Ho, S. P., Jarosik, N., Page, L. A., Parker, L. P., Raghunathan, S., Simon, S. M., Staggs, S. T., and Visnjic, K., "Systematic effects from an ambient-temperature, continuously rotating half-wave plate," *Review of Scientific Instruments* **87**, 094503 (Sept. 2016).

[10] Takakura, S., Aguilar, M., Akiba, Y., Arnold, K., Baccigalupi, C., Barron, D., Beckman, S., Boettger, D., Borrill, J., Chapman, S., Chinone, Y., Cukierman, A., Ducout, A., Elleflot, T., Errard, J., Fabbian, G., Fujino, T., Galitzki, N., Goeckner-Wald, N., Halverson, N. W., Hasegawa, M., Hattori, K., Hazumi, M., Hill, C., Howe, L., Inoue, Y., Jaffe, A. H., Jeong, O., Kaneko, D., Katayama, N., Keating, B., Keskitalo, R., Kisner, T., Krachmalnicoff, N., Kusaka, A., Lee, A. T., Leon, D., Lowry, L., Matsuda, F., Matsumura, T., Navaroli, M., Nishino, H., Paar, H., Peloton, J., Poletti, D., Puglisi, G., Reichardt, C. L., Ross, C., Siritanasak, P., Suzuki, A., Tajima, O., Takatori, S., and Teply, G., "Performance of a continuously rotating half-wave plate on the POLARBEAR telescope," *Journal of Cosmology and Astroparticle Physics* **2017**, 008 (May 2017).

[11] Pisano, G., Ritacco, A., Monfardini, A., Tucker, C., Ade, P. A. R., Shitvov, A., Benoit, A., Calvo, M., Catalano, A., Goupy, J., Leclercq, S., Macias-Perez, J., Andrianasolo, A., and Ponthieu, N., "Development and application of metamaterial-based Half-Wave Plates for the NIKA and NIKA2 polarimeters," *arXiv e-prints* , arXiv:2006.12081 (June 2020).

[12] Gordon, S., Dober, B., Sinclair, A., Rowe, S., Bryan, S., Mauskopf, P., Austermann, J., Devlin, M., Dicker, S., Gao, J., Hilton, G. C., Hubmayr, J., Jones, G., Klein, J., Lourie, N. P., McKenney, C., Nati, F., Soler, J. D., Strader, M., and Vissers, M., "An Open Source, FPGA-Based LeKID Readout for BLAST-TNG: Pre-Flight Results," *Journal of Astronomical Instrumentation* **5**, 1641003 (Dec. 2016).

[13] Gordon, S., Sinclair, A., Mauskopf, P., Coppi, G., Devlin, M., Dober, B., Fissel, L., Galitzki, N., Gao, J., Hubmayr, J., Lourie, N., Lowe, I., McKenney, C., Nati, F., and Romualdez, J., "Preflight Detector Characterization of BLAST-TNG," *Journal of Low Temperature Physics* **200**, 400–406 (Apr. 2020).

[14] Paiella, A., Battistelli, E. S., Castellano, M. G., Colantoni, I., Columbro, F., Coppolecchia, A., D'Alessandro, G., de Bernardis, P., Gordon, S., Lamagna, L., Mani, H., Masi, S., Mauskopf, P., Pettinari, G., Piacentini, F., and Presta, G., "Kinetic Inductance Detectors and readout electronics for the OLIMPO experiment," in [*Journal of Physics Conference Series*], *Journal of Physics Conference Series* **1182**, 012005 (Feb. 2019).

[15] Vissers, M. R., Austermann, J. E., Malnou, M., McKenney, C. M., Dober, B., Hubmayr, J., Hilton, G. C., Ullom, J. N., and Gao, J., "Ultrastable millimeter-wave kinetic inductance detectors," *Applied Physics Letters* **116**, 032601 (Jan. 2020).